Research Article | Vol. 27, No. 21 / 14 October 2019 / Optics Express 30741
Optics EXPRESS

High-performance racetrack resonator in silicon nitride - thin film lithium niobate hybrid platform

ABU NAIM R. AHMED,* SHOUYUAN SHI, ANDREW J. MERCANTE, AND DENNIS W. PRATHER

Electrical and Computer Engineering Department, University of Delaware, Newark, DE 19716, USA
naimece@udel.edu

Abstract: In this paper, we propose an electro-optic modulator design in a hybrid Si_3N_4-*X*-cut $LiNbO_3$. The modulator is based on a modified racetrack resonator and performs at both DC and heightened frequencies. Here the driving electrodes are defined along the straight section of the racetrack. This is done to maximize modulation and minimize modulation-cancelation that occurs in a conventional *X-cut* $LiNbO_3$-based resonator due to the directional change of the electric field in the micro-ring. The single bus racetrack resonator is formed in a hybrid Si_3N_4-$LiNbO_3$ platform, to guide the optical mode. The fabricated device is characterized and has a measured tunability and intrinsic quality factor (Q) of 2.9 pm/V and 1.3×10^5, respectively. In addition, the proposed racetrack device exhibits enhanced electro-optic conversion efficiency at modulation frequencies that match with the racetrack's optical free spectral range (FSR). For example, at the modulation frequency of 25 GHz, which corresponds to the fabricated device's optical FSR frequency, a ~10 dB increase in electro-optic conversion efficiency is demonstrated. With the enhancement, our measured device demonstrates a conversion efficiency comparable to non-resonant thin-film $LiNbO_3$ devices that possess RF electrodes that are 10 times longer in length.

1. Introduction

The micro-resonator has become a key building block in photonic integrated circuits (PICs), with applications spanning from microwave photonics to quantum computing, and high sensitivity sensors [1,2]. It offers various functionalities such as optical switching, filtering, high-speed modulation, wavelength division multiplexing (WDM) and frequency comb generation on a chip-scale [3]. The crystal ion sliced (CIS) thin-film $LiNbO_3$-based standalone and hybrid photonic platforms (heterogeneous integration of $LiNbO_3$ with other materials) have drawn significant attention within the research community because of its tight optical mode confinement resulting low voltage operation, low drive power, and compact footprint. [4–16]. In addition, silicon-based micro-rings have been widely investigated [17–21]. However, due to the intrinsic properties of silicon, the application of these devices has been limited by its nonlinear response, temperature sensitivity and high insertion loss [22–24]. The Si_3N_4-$LiNbO_3$ hybrid platform has recently been investigated with great potential due to its superior optical properties and the versatile functionality [6–8,24]. This hybrid material system combines the strong linear electro-optic (EO) effect in $LiNbO_3$ with the ultra-low propagation loss, low second-order nonlinearity, small thermo-optic coefficient, high power handling capability, and wide optical transparency window of Si_3N_4 [24,25], to achieve low optical insertion loss, low nonlinearity due to plasma dispersion, ultra-fast modulation and low voltage operation compared to alternative methods. Furthermore, a strip-loaded Si_3N_4 waveguide on thin-film $LiNbO_3$ allows for an etch free $LiNbO_3$ modulator fabrication. Lastly, the highly confined optical mode together with closely placed RF electrodes significantly reduces the driving voltage required for electro-optic tuning. In general, the electrodes are placed along an optical micro-ring resonator [7,18,26,27], however, in an *X*-cut $LiNbO_3$, the EO effect in r_{33} crystal orientation dominates. As a result, such

#374024 https://doi.org/10.1364/OE.27.030741
Journal © 2019 Received 29 Jul 2019; revised 29 Aug 2019; accepted 26 Sep 2019; published 9 Oct 2019

Optics EXPRESS

a ring structure would fail to take full advantage of r_{33} due to the change in crystal direction along the optical waveguide path in the resonator [7]. Thus, to attain optimal modulation, the resonator structure needs to be modified to maximize the use of r_{33} and provide a strong modal overlap between the RF signal and the fundamental transverse electric (TE) optical mode. Recently, modified micro-ring electrode design has been demonstrated in standalone *X*-cut $LiNbO_3$ [24,28] and hybrid *X*-cut ChG-$LiNbO_3$ platform [23]. However, hybrid Si_3N_4-$LiNbO_3$ platform remains unexplored. Furthermore, high-frequency operation and RF modulation enhancement using FSR coupling [29,30] of micro-ring on this hybrid platform have yet to be studied.

In this paper, we demonstrate a PECVD Si_3N_4-*X-cut* $LiNbO_3$-based modified hybrid racetrack resonator where the modulating electrodes are placed on both sides of the long arm of the racetrack so that only the r_{33} Pockels coefficient is utilized for resonant wavelength tuning/modulation. The modified structure efficiently utilizes the maximum EO coefficient and thereby improves the tunability by a factor of 1.6 over that of conventional micro-ring resonators [7]. A high intrinsic Q-factor of 1.3×10^5 and racetrack loss of 0.2 dB/cm are calculated for this modified structure. The demonstrated device shows a low $V_\pi L$, high modulation efficiency, and high linearity. The device is characterized electrically up to 32 GHz RF frequencies, thus demonstrating high RF modulation efficiency. An enhanced modulation efficiency of about 10 dB is observed when the modulated optical sidebands are coupled to the adjacent free spectral range (FSR) modes [29,30]. This paper is organized by first presenting the design and fabrication of the modified structure, followed by the racetrack resonator transmission and DC characterization. Subsequently, high-frequency modulation and modulation efficiency are compared with a micro-ring resonator and the effect of FSR coupled-mode on the racetrack is discussed.

2. Device design and fabrication

A schematic of the proposed hybrid racetrack resonator is shown in Fig. 1(a). The hybrid waveguide core is formed by depositing a 200 nm plasma-enhanced chemical vapor deposition (PECVD) Si_3N_4 strip on top of the 300 nm *X*-cut thin-film $LiNbO_3$ overlaid with a 2 μm SiO_2 bottom cladding layer. The thickness and width of the Si_3N_4 strip are 200 nm and 1.2 μm, respectively. The dimensions are chosen to only support the fundamental TE mode that offers a bending loss of less than 0.01 dB/90° bend, 300 μm radii are used for all bends in this device. The mode confinement factor in the $LiNbO_3$ is ~ 65% for this configuration [7]. The inset in Fig. 1(a) shows the field distribution of the fundamental TE mode in the straight waveguide section. The modulated racetrack consists of a 1.5 mm long (L_{Probe}) straight section, three half circles, and two S-shaped bends; with the same bending radius of 300 μm. After etching the Si_3N_4 the parallel plate driving electrodes are patterned on the top of the exposed *X*-cut $LiNbO_3$ film. The racetrack straight arm is centered within the electrodes' 6 μm gap. The racetrack is designed such that the device conserves the optical quality factor (bus to racetrack coupling coefficient, absorption loss) and maintains maximum electro-optic interaction (see Appendix). An optical microscope image of the fabricated device is shown in Fig. 1(b).

Figure 2(a) shows the cross-section schematic of the complete fabrication steps. The fabrication process involves three main critical steps: (i) thin-film Si_3N_4 (200 nm) deposition by PECVD, (ii) optical waveguide and resonator patterning by e-beam lithography (EBL) and dry etching, and (iii) electrode definition by direct laser lithography. The fabrication steps are performed on the thin-film *X*-cut CIS $LiNbO_3$ on insulator (LNOI), which is procured from NanoLN. The 3" LNOI wafer consists of a 300 nm thick layer of the *X*-cut $LiNbO_3$ layer, bonded to a 500 μm thick quartz handle wafer via a 2 μm PECVD SiO_2 intermediate layer. The hybrid material platform is realized by depositing a thin-film Si_3N_4 on the top of the LNOI substrate. A 200 nm of PECVD Si_3N_4 is deposited using the following parameters: SiH_4 (10 sccm)/ NH_3(6 sccm)/N_2 (300 sccm), chamber pressure of 100 Pa, RF power of 50 W, and temperature of 300°C. The refractive index is 1.943 at 1550 nm, measured by an ellipsometer and the deposition rate is ~42

Optics EXPRESS

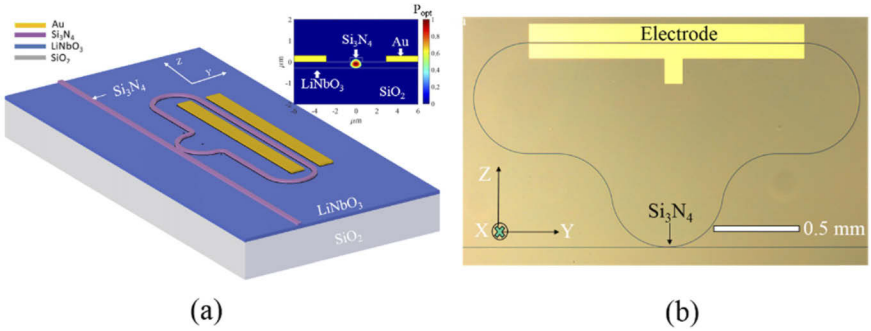

Fig. 1. (a) Schematic of the tunable hybrid Si_3N_4-$LiNbO_3$ racetrack resonator with integrated electrodes (not drawn to scale). Simulated TE optical mode-field profile of a hybrid Si_3N_4-$LiNbO_3$ waveguide formed by a 200 nm × 1.2 µm Si_3N_4 loading strip at 1550 nm (inset). (b) Microscope image of the hybrid Si_3N_4-$LiNbO_3$ racetrack resonator with integrated electrodes.

nm/min. To define the optical waveguide, an 80 nm thick chromium (Cr) layer is sputtered onto the insulating substrate. The Cr layer acts as a conducting layer to mitigate charging phenomenon during EBL. A soft-mask of the optical waveguide and resonators are defined by EBL writing on AR-N 7520.18 negative tone resist, the patterns are aligned in such a way that light propagates along the crystal *Y*-axis, this ensures maximum access to the r_{33} electro-optic coefficient. The soft-mask patterns are then transferred into the Cr hard-mask with Cl [(45 sccm)/O_2 (2 sccm)] based inductively coupled plasma (ICP) dry etching and subsequently into the Si_3N_4 thin-film using an Fl based ICP. The following parameters are used for pattern transfer into Si_3N_4: SF_6 (5 sccm) / C_4F_8 (5 sccm)/ Ar (90 sccm), chamber pressure of 1.5 Pa, RF plasma power of 500 W and DC bias power of 150 W. The etch rate of Si_3N_4 is ~2.6 nm/sec. The remaining EBL resist on the sample was removed by oxygen plasma cleaning followed by piranha wet cleaning [H_2SO_4 (75%): H_2O_2 (25%)] at 80°C for 2 minutes. Finally, the remaining Cr is stripped in a chemically selective wet etch and followed by a 3-minutes piranha and oxygen plasma clean. This cleaning process strips the residual resist and insoluble particles that are stuck to the waveguide sidewalls. Finally, Coplanar Stripline (CPS) electrodes are defined on the top surface of the $LiNbO_3$ layer. A bilayer lift-off process is performed to transfer the electrode mask onto the soft-mask to obtain a clean solvent lift-off. The lift-off resists LOR-5A (MicroChemicals) is coated first, followed by the positive tone AZ 1512 (MicroChemicals) coating. A direct laser writer (Heidelberg MLA 100) is used to perform lithography, which maintains high-precision alignment of the electrode placement with the optical structure. The photoresists are developed simultaneously with AZ 300 MIF developer (MicroChemicals) for 2 minutes. An oxygen plasma is performed to strip residual resist and to promote metal adhesion of the subsequently deposited metal layers. Electron beam evaporation is used to put down 20 nm of Ti followed by 350 nm of Au. Metal lift-off is performed in NMP solvent (1-methyl-2-pyrrolidinone) at 80°C in the ultrasonic bath for 15 minutes. Devices are then diced, and the facets are polished at ~15° top to bottom angle to ensure low fiber-chip coupling loss. The fabricated device with integrated electrodes is shown in Figs. 2(b) and 2(c).

Optics EXPRESS

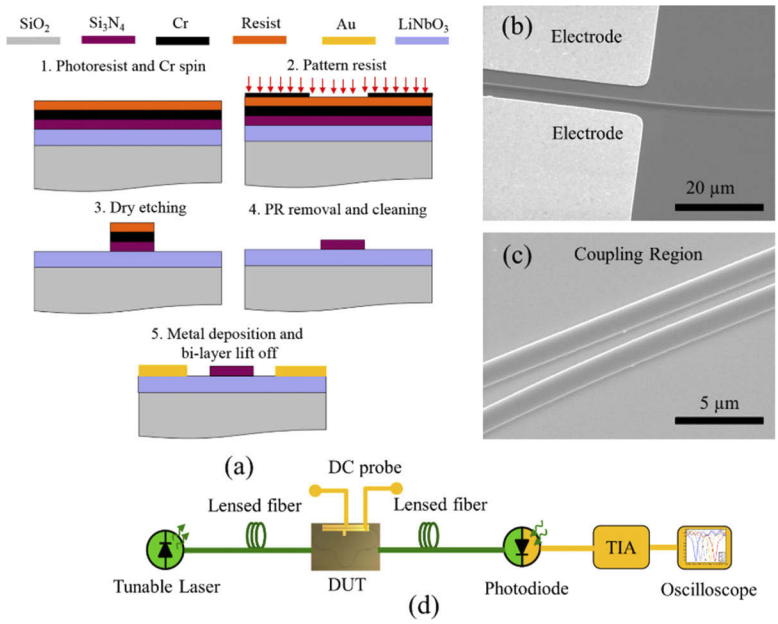

Fig. 2. (a) Schematic of the fabrication flow of the hybrid Si_3N_4-$LiNbO_3$ based racetrack device (b) SEM image of the fabricated racetrack resonator (c) Close-up SEM image of the evaporated electrode and optical waveguide (d) Close-up SEM image of the racetrack coupling (e) Experimental setup for the racetrack transmission and DC tuning characterization. The green line indicates the optical domain and the yellow line indicates the electrical domain.

3. Racetrack optical transmission and DC characterization

The transmission spectrum of the modified racetrack resonator is extracted using a tunable laser (Keysight 81608 A) swept at wavelengths around 1550 nm. The experimental setup of the measurement is shown in Fig. 2(d). The input and output optical light is coupled to the device under test (DUT) using a ~ 2 µm spot size, TE-polarized tapered lensed fiber. The output light is detected by an InGaAs photodetector (DET08CFC) and directed to an oscilloscope via a trans-impedance amplifier (TIA). The measured spectrum of the modified hybrid racetrack resonator around 1550 nm is shown in Fig. 3(a). The spectrum exhibits periodic dips with uniform spacing between the adjacent resonating dips. The loaded quality factor of ~ 6.5×10^4 is extracted at 1550.108 nm by fitting the central transmission dip with a Lorentzian model [31] as depicted in Fig. 3(b). The corresponsing intrinsic quality factor is ~ $1.3\,x10^5$ [31]. The measured linewidth and free spectral range (FSR) are $\delta\lambda_{FWHM} = 0.0242$ nm and $\Delta\lambda_{FSR} = 0.207$ nm, respectively. The propagation loss per unit length in the modified racetrack is calculated as ~ 0.2 dB/cm [31]. The total optical insertion loss for this device is ~13 dB, mainly attributed to the mode mismatch between the optical waveguide and input fiber. The tunability of the modified racetrack device is measured by applying a varied DC voltage to the driving electrodes and measuring the corresponding resonance wavelength shift. The applied DC voltage modifies the optical path length due to the change of the refractive index, causing a shift of the resonance wavelength. The DC voltage is applied to the racetrack's integrated electrodes using a DC source and a DC needle probe. The wavelength tuning spectra at different voltages are shown in Fig. 3(c). The resonance wavelength shifts by ~ 72.75 pm from the resonance wavelength 1550.108 nm as the voltage are swept from 0 V to 25 V, demonstrating a wavelength tunability ($\delta\lambda/\delta V$) of ~ 2.9 pm/V. The achieved tunability is 1.6 times better than that of our previous micro-ring based resonator

Optics EXPRESS

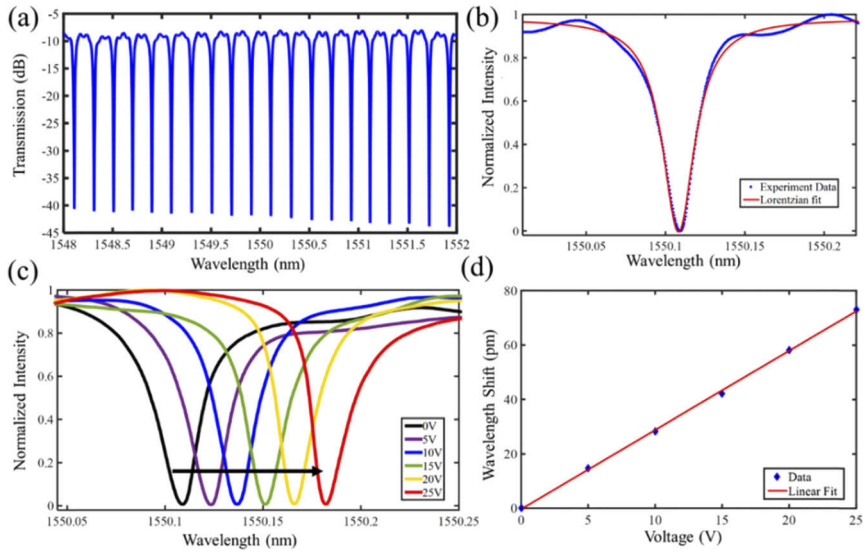

Fig. 3. (a) The measured transmission spectrum of the passive racetrack resonator at the through port for the TE mode using a tunable laser near 1550 nm. The free spectral range is measured to be 0.2 nm. (b) The Lorentz fitting (red curve) of the resonance dip at 1550.108 nm which corresponds to an intrinsic Q of 7.68×10^5. (c) The spectrum resonant shift for different DC voltages for TE mode at wavelength 1550.108 nm (black curve) of the racetrack resonator. The shift indicated a tunability of 2.9 pm/V. (d) Resonant wavelength shift as a function of the applied DC voltage shows excellent linearity.

[7]. The racetrack resonator also exhibits good linear dependence of the wavelength shift on the applied voltage as shown in Fig. 3(d). The DC modulation efficiency ($V_\pi L$) of the racetrack resonator is also calculated using the following equation, $V_\pi L = (0.5 * L_{Probe} * FSR)/(\delta\lambda/\delta V)$ [32]. The calculated $V_\pi L$ of the modified racetrack resonator is 5.1 V·cm.

4. High-frequency characterization

To characterize the high-frequency response of the micro-ring and modified racetrack resonator configurations, we examine the generated peak sidebands that appear under the application of a modulating RF signals. The sidebands are offset from the input optical carrier by an equivalent to the applied modulation frequency. The setup used for sideband measurement is shown in Fig. 4(a). An RF electrical signal is fed from a signal generator (N5183A MXG) to the device electrode using a standard 50 Ω impedance ground-signal (GS) configuration probe (GGB industries) with a 67 GHz operational bandwidth. The optical signal is coupled into the DUT directly from the tunable laser via a TE polarized lensed fiber. The modulated optical signal is directly fed into a Yokogawa AQ5319 Optical Spectrum Analyzer (OSA) and the intensity of the observed modulation sidebands is recorded for each applied RF frequency. The modulation spectra are normalized to the measured power of the carrier at the off-resonant frequency of the resonator. The optical sideband normalization accounts for probe insertion loss and feed loss. Normalized modulation spectra for the modified racetrack and micro-ring are shown in Figs. 4(b) and 4(c), respectively. The normalized sidebands are plotted at 2 GHz increments for each device. The broad peak located at the center of the spectra corresponds to the laser wavelength, which lies in the slope of the resonance curve. The colored peaks on both sides of the center peaks are the modulation sidebands. The laser carrier wavelength is chosen such that the frequency detuning (optical frequency detuning of the laser from the mirroring resonance)

Optics EXPRESS

is equal to ~ 0.58 times of the half width at half max (HWHM) bandwidth of the resonator, which is considered as optimal detuning for maximum gain [33]. In the racetrack modulator, the sideband rolls-off as the RF modulation frequency (f_m) remains within $FWHM < f_m < FSR$. The sidebands increase around adjacent resonances and approach a local maximum at ~25 GHz: the FSR of the racetrack. This is due to both the sideband and optical carrier frequencies being resonant in the cavity simultaneously. The generated sidebands are transmitted through the ring, which increases the modulation efficiency [29,32] and the sideband power is increased by 9.5 dB as f_m sweeps from 8 GHz to 25 GHz. The sideband power of the micro-ring resonator is also examined up to 32 GHz as shown in Fig. 4(c). Here the micro-ring is surrounded by the electrode (L_{probe} = ~1.5 mm) except the bus to the ring coupling region. In the micro-ring resonator, the sideband power rolls-off as frequencies increases upto 32 GHz, modulation enhancement is not observed since the modulation frequency remains below the FSR frequency of the ring (~70 GHz). Here, the generated sidebands are not resonant in the ring, therefore the modulation efficiency decreases. At the modulation frequency of 8 GHz, the modified racetrack modulation efficiency is ~10.32 dB higher than that of the micro-ring resonator, as shown in Fig. 5(a). These results indicate that for the same electrode length, the modified racetrack resonator structure improves the DC tunability, modulation efficiency, and energy consumption significantly. Besides, the modulation efficiency is comparable to the long thin film $LiNbO_3$ phase modulator [16]. The CPS transmission characteristics of the racetrack are measured using a vector network analyzer (VNA) up to 67 GHz. The VNA was calibrated using Short-

Open-Load-Thru (SOLT) standards using calibration substrate 8 (CS8) from GGB. Ground-Signal probes were used for both the signal launch and terminated. The high-speed performance of the modulator devices depends on impedance matching of the CPS to the source impedance [34] and RF and optical index mismatch [34]. In Fig. 5(b), the electrical transmission (S21) shows a smooth trend up to 67 GHz and the loss is close to 0 dB due to the short electrical length, the trend also matches with the simulated S21 (see Appendix). The electrical return loss (S11) is below ~12 dB upto 67 GHz indicating that the impedance is likely near 50 Ω. From the S-parameter measurement [35], the characteristic impedance and the RF group index (n_{RF}) of the integrated racetrack electrodes have been estimated to be ~ 58 Ω and 2.09, respectively. From the

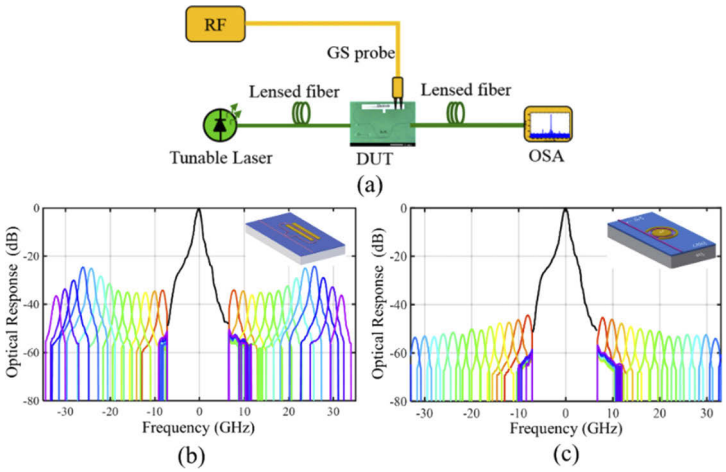

Fig. 4. (a) Experimental setup for high-speed modulation. The normalized optical modulation spectra of the (b) modified racetrack modulator, and (c) standard micro-ring modulator with RF sinusoids at different frequencies. The inset shows the pictorial view of the respective modulator. The frequency detuning is chosen to ensure optimal gain for both modulators.

Optics EXPRESS

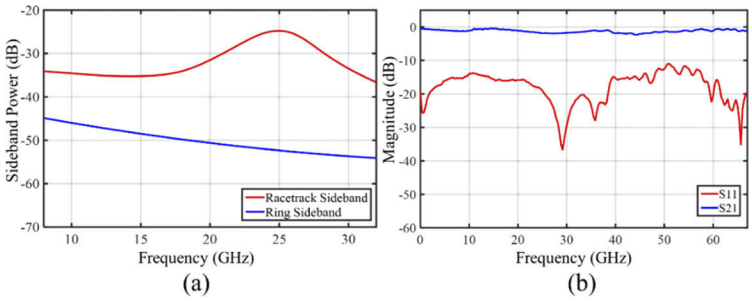

Fig. 5. (a) The normalized sideband power of the racetrack modulator (red) and standard micro-ring modulator (blue). The sideband power is calibrated to exclude the RF cable loss and probe loss. (b) Measured transmission (S21) and reflected coefficient (S11) of the fabricated CPS electrode configuration.

simulated optical group index (n_{opt}), the modal effective index mismatch for this type of electrode is ~0.08. The modulation efficiency can be further improved by optimizing the device electrode design (e.g. electrode gap, height, and RF cavity) [30,34,36]. Extended operational frequency is achievable by modifying the optical path length, such that the resonator FSR matches with the operating frequency [30]. The optical loss can be further improved by introducing a glass cladding layer and using low-pressure chemical vapor deposition (LPCVD) Si_3N_4 instead of PECVD Si_3N_4, reducing the hydrogen content in the Si_3N_4 [37–39]. Future work will require an investigation of an efficient edge coupling into and out of the optical waveguide by introducing either a mode transition structure using inverse taper or a grating coupler [40,41].

5. Conclusion

In summary, a tunable modified racetrack resonator is demonstrated using a Si_3N_4-$LiNbO_3$ hybrid platform that exhibits a high intrinsic Q factor of 1.3×10^5 along with high resonance tunability of 2.9 pm/V. The modified racetrack design in both optical and electrical domains offers maximum utilization of the electro-optic coefficient of $LiNbO_3$ to the resonant structure, thereby achieving enhanced modulation efficiency compared to a micro-ring resonator. Our modified racetrack resonator also exhibits higher modulation efficiency (~10 dB) when coupled to the adjacent FSR resonance modes. To the best of our knowledge, this is the first demonstration of the FSR coupled-mode resonance-based high-frequency modulation in hybrid Si_3N_4 strip loaded thin-film $LiNbO_3$ platform. This unique device also exhibits excellent linearity, low voltage operation, banded modulation (can operate at n^{th} adjacent resonance mode), low resonator optical loss, and compact optical modulation.

Appendix: Simulation results of the racetrack modulator

The single TE mode optical waveguide was designed in Lumerical Mode solver software. The optimal device dimensions are chosen to be maximizing the mode confinement in the $LiNbO_3$ and minimizing optical bending loss. The detail results were shown in our previous work [7]. The racetrack structure on the hybrid Si_3N_4-$LiNbO_3$ platform is simulated using

2.5-D variational finite difference time domain simulations (varFDTD) from Lumerical solutions. The transmission spectrum of the simulated microresonator is shown in Fig. 6(a). The resonance peak near 1550.115 nm is fitted with a Lorentzian as shown in Fig. 6(b). The simulated linewidth and the free spectral range are $\delta\lambda_{FWHM} = 0.021$ nm and $\Delta\lambda_{FSR} = 0.208$ nm, respectively. The simulated result agrees well with the measured data. The linewidth variation might occur due to the additional losses in the fabricated waveguide. The loaded Q of the simulated micro-ring is

Optics EXPRESS

~7.4×10^4, which is higher than our measured loaded Q of 6.5×10^4 due to the additional losses in the waveguide. Another most critical factor for this type of modulator design is the effect of the electrode gap on the micro-ring quality factor. To maximize the modulation efficiency, a small electrode gap is desired. However, closely placed metal electrodes induce an additional absorption loss in the optical waveguide. As a result, the closely placed metals reduce the quality factor of the micro-ring. The metal-induced absorption loss for different electrode gaps is calculated in Lumerical MODE solutions. From Fig. 7(a), the absorption loss is significantly higher below 5.5 µm electrode gap, while the loss is nearly unchangeable above 5.5 µm electrode gap. The effect of the electrode gap on the intrinsic quality factor has experimentally measured. Figure 7(b) shows intrinsic quality factor ascending with increasing electrode gap, and it remained constant when the electrode gap reached to 6 µm. Thus, a 6 µm electrode gap is chosen for designing the CPS electrode and maintaining an acceptable metal absorption loss. The electric field distribution of our designed electrode is simulated with ANSYS High Frequency Structure Simulation (HFSS). The electric field map and the field profile of the device in contact with the probe are shown at Figs. 8(a) and 8(b). The electrical field along the optical waveguide is extracted. The simulated field illustrated about ~9.8×10^4 V/m. The cross-sectional view of the simulated optical TE mode profile and the electric field directions (arrows) between the electrodes is shown in Fig. 9(a). Finally, the simulated S-parameters of the designed CPS is shown in Fig. 9(b).

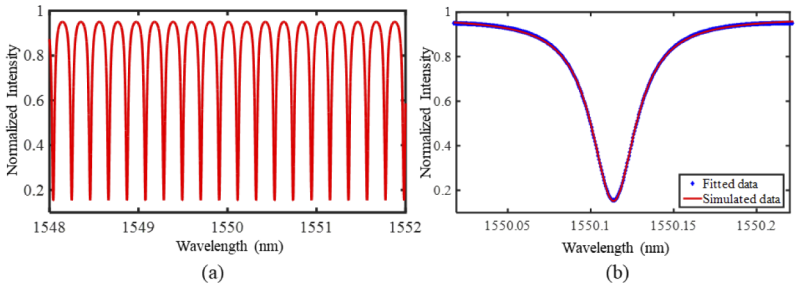

Fig. 6. (a) The simulated transmission spectrum of the passive racetrack resonator at the through port for the TE mode (b) The Lorentz fitting (blue curve) of the resonance dip at 1550.115 nm.

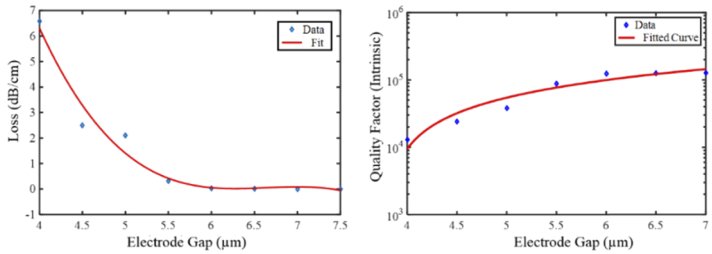

Fig. 7. (a) Simulated absorption loss as a function of the electrode gap. (b) Experiment result of the intrinsic quality factor variation with the electrode gap.

Optics EXPRESS

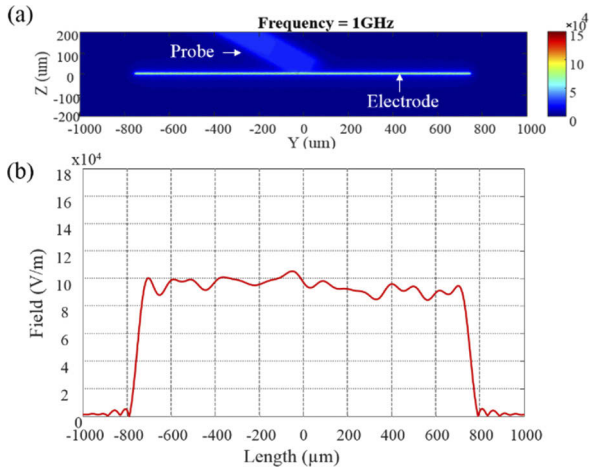

Fig. 8. (a) HFSS simulated electric field distribution over the entire electrode length for a 6 μm electrode gap at 1 GHz. (b) The simulated electric field plotted along the entire length of the electrode at 1 GHz.

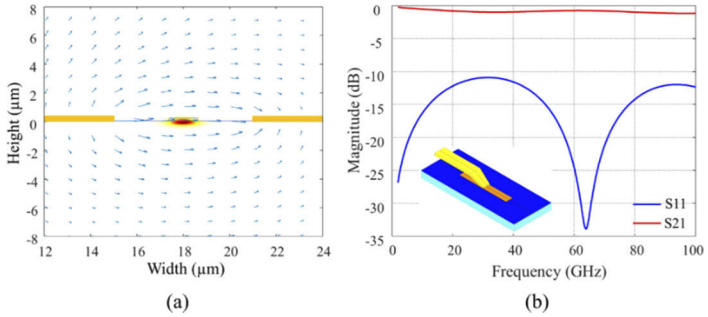

Fig. 9. (a) Simulated electric field direction (blue arrow) between the two electrodes and inside the optical waveguide region. (b) Simulated S-parameters extracted from the HFSS model.

Funding

Air Force Office of Scientific Research (FA9550-17-1-0071).

Acknowledgments

The authors acknowledge support from the Multidisciplinary University Research Initiative (MURI) program through the Air Force Office of Scientific Research (AFOSR), program managed by Dr. Gernot Pomrenke.

References

1. Z. Yao, K. Wu, B. X. Tan, J. Wang, Y. Li, Y. Zhang, and A. W. Poon, "Integrated silicon photonic microresonators: Emerging Technologies," IEEE J. Sel. Top. Quantum Electron. **24**(1), 1–11 (2018).
2. J. W. Silverstone, R. Santagati, D. Bonneau, M. J. Strain, M. Sorel, J. L. O'Brien, and M. G. Thompson, "Qubit entanglement between ring-resonator photon-pair sources on a silicon chip," Nat. Commun. **6**(1), 7948 (2015).
3. W. Bogaerts, P. De Heyn, T. Van Vaerenbergh, K. De Vos, S. Kumar Selvaraja, T. Claes, P. Dumon, P. Bienstman, D. Van Thourhout, and R. Baets, "Silicon microring resonators," Laser Photonics Rev. **6**(1), 47–73 (2012).
4. A. Boes, B. Corcoran, L. Chang, J. Bowers, and A. Mitchell, "Status and Potential of Lithium Niobate on Insulator (LNOI) for Photonic Integrated Circuits," Laser Photonics Rev. **12**(4), 1700256 (2018).

Optics EXPRESS

5. P. O. Weigel, M. Savanier, C. T. DeRose, A. T. Pomerene, A. L. Starbuck, A. L. Lentine, V. Stenger, and S. Mookherjea, "Lightwave circuits in lithium niobate through hybrid waveguides with silicon photonics," Sci. Rep. **6**(1), 22301 (2016).
6. L. Chang, M. H. Pfeiffer, N. Volet, M. Zervas, J. D. Peters, C. L. Manganelli, E. J. Stanton, Y. Li, T. J. Kippenberg, and J. E. Bowers, "Heterogeneous integration of lithium niobate and silicon nitride waveguides for wafer-scale photonic integrated circuits on silicon," Opt. Lett. **42**(4), 803–806 (2017).
7. A. N. R. Ahmed, S. Shi, M. Zablocki, P. Yao, and D. W. Prather, "Tunable hybrid silicon nitride and thin-film lithium niobate electro-optic microresonator," Opt. Lett. **44**(3), 618–621 (2019).
8. A. N. R. Ahmed, A. Mercante, S. Shi, P. Yao, and D. W. Prather, "Vertical mode transition in hybrid lithium niobate and silicon nitride-based photonic integrated circuit structures," Opt. Lett. **43**(17), 4140–4143 (2018).
9. S. Jin, L. Xu, H. Zhang, and Y. Li, "LiNbO 3 thin-film modulators using silicon nitride surface ridge waveguides," IEEE Photonics Technol. Lett. **28**(7), 736–739 (2016).
10. A. Rao and S. Fathpour, "Compact lithium niobate electrooptic modulators," IEEE J. Sel. Top. Quantum Electron. **24**(4), 1–14 (2018).
11. Y. Wang, Z. Chen, L. Cai, Y. Jiang, H. Zhu, and H. Hu, "Amorphous silicon-lithium niobate thin film strip-loaded waveguides," Opt. Mater. Express **7**(11), 4018–4028 (2017).
12. C. Wang, M. Zhang, B. Stern, M. Lipson, and M. Lončar, "Nanophotonic lithium niobate electro-optic modulators," Opt. Express **26**(2), 1547–1555 (2018).
13. M. He, M. Xu, Y. Ren, J. Jian, Z. Ruan, Y. Xu, S. Gao, S. Sun, X. Wen, and L. Zhou, "High-performance hybrid silicon and lithium niobate Mach–Zehnder modulators for 100 Gbit s-1 and beyond," Nat. Photonics **13**(5), 359–364 (2019).
14. A. Guarino, G. Poberaj, D. Rezzonico, R. Degl'Innocenti, and P. Günter, "Electro–optically tunable microring resonators in lithium niobate," Nat. Photonics **1**(7), 407–410 (2007).
15. P. O. Weigel, J. Zhao, K. Fang, H. Rubaye, D. Trotter, D. Hood, J. Mudrick, C. Dallo, A. T. Pomerene, A. L. Starbuck, C. T. DeRose, A. L. Lentine, G. Rebeiz, and S. Mookherjea, "Bonded thin film lithium niobate modulator on a silicon photonics platform exceeding 100 GHz 3-dB electrical modulation bandwidth," Opt. Express **26**(18), 23728–23739 (2018).
16. A. J. Mercante, S. Shi, P. Yao, L. Xie, R. M. Weikle, and D. W. Prather, "Thin film lithium niobate electro-optic modulator with terahertz operating bandwidth," Opt. Express **26**(11), 14810–14816 (2018).
17. Y. S. Lee, G.-D. Kim, W.-J. Kim, S.-S. Lee, W.-G. Lee, and W. H. Steier, "Hybrid Si-LiNbO 3 microring electro-optically tunable resonators for active photonic devices," Opt. Lett. **36**(7), 1119–1121 (2011).
18. L. Chen, M. G. Wood, and R. M. Reano, "12.5 pm/V hybrid silicon and lithium niobate optical microring resonator with integrated electrodes," Opt. Express **21**(22), 27003–27010 (2013).
19. J. D. Witmer, J. A. Valery, P. Arrangoiz-Arriola, C. J. Sarabalis, J. T. Hill, and A. H. Safavi-Naeini, "High-Q photonic resonators and electro-optic coupling using silicon-on-lithium-niobate," Sci. Rep. **7**(1), 46313 (2017).
20. J. Chiles and S. Fathpour, "Mid-infrared integrated waveguide modulators based on silicon-on-lithium-niobate photonics," Optica **1**(5), 350–355 (2014).
21. P. Rabiei, J. Ma, S. Khan, J. Chiles, and S. Fathpour, "Heterogeneous lithium niobate photonics on silicon substrates," Opt. Express **21**(21), 25573–25581 (2013).
22. M. Mahmoud, L. Cai, C. Bottenfield, and G. Piazza, "Lithium niobate electro-optic racetrack modulator etched in Y-cut LNOI platform," IEEE Photonics J. **10**(1), 1–10 (2018).
23. A. Rao, A. Patil, J. Chiles, M. Malinowski, S. Novak, K. Richardson, P. Rabiei, and S. Fathpour, "Heterogeneous microring and Mach-Zehnder modulators based on lithium niobate and chalcogenide glasses on silicon," Opt. Express **23**(17), 22746–22752 (2015).
24. K. Alexander, J. P. George, J. Verbist, K. Neyts, B. Kuyken, D. Van Thourhout, and J. Beeckman, "Nanophotonic Pockels modulators on a silicon nitride platform," Nat. Commun. **9**(1), 3444 (2018).
25. R. Baets, A. Z. Subramanian, S. Clemmen, B. Kuyken, P. Bienstman, N. Le Thomas, G. Roelkens, D. Van Thourhout, P. Helin, and S. Severi, "Silicon Photonics: silicon nitride versus silicon-on-insulator," in *Optical Fiber Communications Conference and Exhibition* (Optical Society of America, 2016), paper Th3J-1.
26. Y. He, H. Liang, R. Luo, M. Li, and Q. Lin, "Dispersion engineered high quality lithium niobate microring resonators," Opt. Express **26**(13), 16315–16322 (2018).
27. C. Wang, M. Zhang, M. Yu, R. Zhu, H. Hu, and M. Loncar, "Monolithic lithium niobate photonic circuits for Kerr frequency comb generation and modulation," Nat. Commun. **10**(1), 978 (2019).
28. M. Zhang, B. Buscaino, C. Wang, A. Shams-Ansari, C. Reimer, R. Zhu, J. M. Kahn, and M. Lončar, "Broadband electro-optic frequency comb generation in a lithium niobate microring resonator," Nature **568**(7752), 373–377 (2019).
29. L. D. Tzuang, M. Soltani, Y. H. D. Lee, and M. Lipson, "High RF carrier frequency modulation in silicon resonators by coupling adjacent free-spectral-range modes," Opt. Lett. **39**(7), 1799–1802 (2014).
30. B. Bortnik, Y.-C. Hung, H. Tazawa, B.-J. Seo, J. Luo, A. K.-Y. Jen, W. H. Steier, and H. R. Fetterman, "Electrooptic polymer ring resonator modulation up to 165 GHz," IEEE J. Sel. Top. Quantum Electron. **13**(1), 104–110 (2007).
31. L.-W. Luo, G. S. Wiederhecker, J. Cardenas, C. Poitras, and M. Lipson, "High quality factor etchless silicon photonic ring resonators," Opt. Express **19**(7), 6284–6289 (2011).

Optics EXPRESS

32. T. Baba, S. Akiyama, M. Imai, N. Hirayama, H. Takahashi, Y. Noguchi, T. Horikawa, and T. Usuki, "50-Gb/s ring-resonator-based silicon modulator," Opt. Express **21**(10), 11869–11876 (2013).
33. V. Van, *Optical Microring Resonators: Theory, Techniques, and Applications* (CRC Press, 2016).
34. E. L. Wooten, K. M. Kissa, A. Yi-Yan, E. J. Murphy, D. A. Lafaw, P. F. Hallemeier, D. Maack, D. V. Attanasio, D. J. Fritz, and G. J. McBrien, "A review of lithium niobate modulators for fiber-optic communications systems," IEEE J. Sel. Top. Quantum Electron. **6**(1), 69–82 (2000).
35. G. L. Li, T. G. B. Mason, and P. K. L. Yu, "Analysis of segmented traveling-wave optical modulators," J. Lightwave Technol. **22**(7), 1789–1796 (2004).
36. D. A. Cohen and A. F. J. Levi, "Microphotonic components for a mm-wave receiver," Solid-State Electron. **45**(3), 495–505 (2001).
37. A. Stoffel, A. Kovacs, W. Kronast, and B. Müller, "LPCVD against PECVD for micromechanical applications," J. Micromech. Microeng. **6**(1), 1–13 (1996).
38. J. F. Bauters, M. J. Heck, D. John, D. Dai, M.-C. Tien, J. S. Barton, A. Leinse, R. G. Heideman, D. J. Blumenthal, and J. E. Bowers, "Ultra-low-loss high-aspect-ratio Si 3 N 4 waveguides," Opt. Express **19**(4), 3163–3174 (2011).
39. M.-C. Tien, J. F. Bauters, M. J. Heck, D. J. Blumenthal, and J. E. Bowers, "Ultra-low loss Si 3 N 4 waveguides with low nonlinearity and high power handling capability," Opt. Express **18**(23), 23562–23568 (2010).
40. L. He, M. Zhang, A. Shams-Ansari, R. Zhu, C. Wang, and M. Loncar, "Low-loss fiber-to-chip interface for lithium niobate photonic integrated circuits," ArXiv Prepr. ArXiv190208969 (2019).
41. Z. Chen, Y. Wang, Y. Jiang, R. Kong, and H. Hu, "Grating coupler on single-crystal lithium niobate thin film," Opt. Mater. **72**, 136–139 (2017).